

Augmented Imagefication: A Data-driven Fault Detection Method for Aircraft Air Data Sensors^{*}

Hang Zhao^a, Jinyi Ma^a, Zhongzhi Li^a, Yiqun Dong^{a,*}, Jianliang Ai^a

^a*Department of Aeronautics and Astronautics, Fudan University, Shanghai 200433, China*

Abstract

In this paper, a novel data-driven approach named Augmented Imagefication for Fault detection (FD) of aircraft air data sensors (ADS) is proposed. Exemplifying the FD problem of aircraft air data sensors, an online FD scheme on edge device based on deep neural network (DNN) is developed. First, the aircraft inertial reference unit measurements is adopted as equivalent inputs, which is scalable to different aircraft/flight cases. Data associated with 6 different aircraft/flight conditions are collected to provide diversity (scalability) in the training/testing database. Then Augmented Imagefication is proposed for the DNN-based prediction of flying conditions. The raw data are reshaped as a grayscale image for convolutional operation, and the necessity of augmentation is analyzed and pointed out. Different kinds of augmented method, i.e. Flip, Repeat, Tile and their combinations are discussed, the result shows that the All_Repeat operation in both axes of image matrix leads to the best performance of DNN. The interpretability of DNN is studied based on Grad-CAM, which provide a better understanding and further solidifies the robustness of DNN. Next the DNN model, VGG-16 with augmented imagefication data is optimized for mobile hardware deployment. After pruning of DNN, a lightweight

^{*}This work was sponsored by Shanghai Sailing Program under Grant No. 20YF1402500.

^{*}Corresponding author.

Email addresses: zhaohang@fudan.edu.cn (Hang Zhao), jyma21@m.fudan.edu.cn (Jinyi Ma), sau_lzz@foxmail.com (Zhongzhi Li), yiqundong@fudan.edu.cn (Yiqun Dong), aijl@fudan.edu.cn (Jianliang Ai)

model (98.79% smaller than original VGG-16) with high accuracy (slightly up by 0.27%) and fast speed (time delay is reduced by 87.54%) is obtained. And the hyperparameters optimization of DNN based on TPE is implemented and the best combination of hyperparameters is determined (learning rate 0.001, iterative epochs 600, and batch size 100 yields the highest accuracy at 0.987). Finally, an online FD deployment based on edge device, Jetson Nano, is developed and the real time monitoring of aircraft is achieved. We believe that this method is instructive for addressing the FD problems in other similar fields.

Keywords: Aircraft Air Data Sensors, Fault Detection, Deep Neural Networks, Data Augmentation, Interpretability Analysis, Online Monitoring

1. Introduction

1.1. Motivation

Fault detection (FD) is crucial for security of service of dynamical systems. Taking aeronautics field as a study case, aircraft air data sensors (ADS) provide measurements of aircraft's airspeed, angle of attack (AOA), and sideslip angle. It is found that the erroneous sensor measurements is the main cause of many catastrophic flight accidents, such as the crashes of NASA X-31 [1], Airbus A330 [2], and recently Boeing B737 MAX [3]. A robust real time fault detection scheme with high performance and reliability in the application is imminent for the health monitoring of commercial airlines.

Nowadays hardware redundancy (HR) is widely used for FD problems. Particularly for ADS in the commercial airlines, HR strategy consists of installing multiple sensors to produce redundant measurements of the air data. Outputs from all the sensors are continuously monitored by a voting logic, which detects (and isolates) the defective sensor. The correct measurement is then reported using the remaining other sensors [4, 5, 6].

There are many shortcomings with the HR-based fault detection, on the one hand, HR leads to high cost of operation and maintenance, on the other hand, the weight penalty (due to the redundant sensors) strategy is needed well

designed for both efficiency and accuracy. Moreover, recent accidents indicate that HR is not sufficient in addressing the fault detection problem (e.g. the Boeing 737MAX accident due to AOA sensors). Alternative to HR, analytical redundancy (AR) has been proposed and investigated[7]. A majority of the AR methods adopted model-based approaches. Different from HR, AR investigates each sensor separately. For a certain sensor, a mathematical model is developed in conjunction with other sensors. An inferred sensor measurement is then estimated and compared with the sensor’s output and the a residual can be generated. If the residual exceeds a predefined bound, then fault is claimed to be detected for that sensor [8].

The model-based AR, nevertheless, hinges on the model that is derived from system specifics, which is sensitive to operational conditions. The development of model-based AR typically requires *ad hoc* parameters tuning, which is time-consuming. Another research line of AR adopts model-free, and mostly data-driven methods. This does not require system specifics, but only the recorded data (e.g. sensors measurements and the associated faults). In particular for the ADS fault detection problem, deep neural networks (DNN) were widely used [9, 10, 11, 12, 13]. However, there is no universal and explainable rule for the architecture devising in DNN, so most works adopt the trial-and-error methodology. Mathematical operations enclosed within the DNN are also considered “black”, scalability of the DNN-based FD scheme is doubtful. Referring to the development of DNN in other fields (e.g. computer vision), many rules and experiences have been proposed and accepted in devising the DNN architectures (e.g. how many CNN filters should be used in each layer). For example, ablation studies [14] of DNN. However, it is very expensive and time-consuming to design such a new DNN with complex structures and mature DNN models is preferable if we can make full use of them. Besides, Many visualization methods of DNN are proposed, e.g., class activation mapping [15], which elevate the understanding of how DNN works. Similar concepts/approaches may also be used in analyzing the DNN-based FD scheme.

We thus summarize the motivation and goals of this paper: develop a DNN-

based methods (existing mature model is preferable) that yield accurate and scalable FD performances, then study the explainability in devising the DNN architecture and interpretability of the DNN operations. Exemplifying the FD problem of aircraft air data sensors, we propose an augmented imagefication method to develop a robust DNN-based FD scheme. Whilst the FD accuracy and scalability must be guaranteed, we also explain the rules in devising the DNN architecture, and interpret the operations enclosed in the DNN structure. Finally we plan to optimize the DNN model to develop an online FD system on edge device and achieve the online monitoring of aircraft conditions.

1.2. Related work

1.2.1. Model-based and Data-driven FD

Previous studies often use model-based approaches, which are sensitive to the specifics of a certain system, attenuating the robustness. Model-based FD hinges on a mathematical model to predict the sensor measurement, which being further used to generate a residual. It is found in a plethora of research literature that Kalman filtering (KF) is widely used. e.g., the extended KF [16, 17, 18], the unscented KF [19], the theoretical analysis of adaptive three-step KF [20], and implementation of the KF-based method to real data in [21]. Other KF-based works included [22, 23], wherein fuzzy logic was used in conjunction with KF to consolidate the sensors data [22], and hidden Markov model has been used to decide the sensors state (fault/healthy) based on the KF outputs in [23]. KF-based FD schemes, however, rely on the evolution model that is derived from the system dynamics/kinematics; *ad hoc* parameters tuning is imminent in adjusting KF to different systems (e.g. different aircraft) or operational cases (e.g. different flight conditions).

Other model-based FD methods adopted robust control theory in [24, 25, 26, 27], wherein the robustness synthesis-based filter was constructed to output the residual. But a sensor state evolution model is needed, and no rules pertaining to the parameters tuning was studied. In [28, 29, 30] moving horizon estimator was developed, which compensated for both sensor faults and wind speed estimation

in the fault tolerant control. However, only limited aircraft/flight cases in these papers are discussed and the scalability of these proposed methods is unclear. A scheme designed particularly for systems with two time-scale dynamics (e.g. phugoid and short periods in the aircraft’s longitudinal plane) was discussed in [31, 32], wherein both nonlinear geometric approach and singular perturbation technique were involved. But computational load of the algorithm was relatively high, and parameters tuning was time-consuming. Barrier function-based learning observer was proposed in [33], and in [34] a set-value observer (SVO) was used. As acclaimed in the papers, these works significantly decreased the FD false alarm rate. The weaknesses of [33] and [34], however, are also typical: model sensitiveness and unclear scalability.

Data-driven methods have claimed accurate performances which scale well to different cases. Most of the data-driven schemes were found to use neural networks (NN). In [9, 10] fully connected cascaded NN was adopted, the authors discussed fault detection and isolation for inertial reference unit (IRU). Similar works were found in [35, 36], wherein feed-forward NN was used. In [37, 38] NN-based adaptive observer was developed to generate the sensor measurement residual; parameters of the NN were adjusted online via KF [37]. Also in [11, 12, 13], NN was used to establish nonlinear identification models, which being used as a state observer to generate the residual. The essence of all these works was to regress a functional relation that maps from the designated input to the desired output (i.e. fault cases). But traditional NN lacks the efficiency in abstracting high-level features. It is usually used in a hybrid form with other methods (e.g. KF). In addition, no research pertaining to the explainability and interpretability analysis was thoroughly illustrated in the associated publications.

Recent NN developments advocate the deep neural networks (DNN) in many academic/industrial fields [39]. DNN typically has more (‘deeper’) layers which are activated using designated function (e.g. ReLU). More dedicated operations were also designed in convolutional neural network (CNN) and long-short time memory (LSTM) blocks for extracting both spatial and temporal features

enclosed in the DNN input. Early works along the DNN-based FD line were found in [40, 41, 42], wherein recurrent neural network (RNN) was used. Later works adopted a variant of RNN, i.e. LSTM, which attenuates the error vanishment/explosion problems in the traditional RNN. CNN was also widely used in conjunction with LSTM. New data formats defined as “state image” and “control image” were proposed in [43, 44], via which the sensor FD accuracy was significantly improved. The CNN-LSTM fusion-based DNN architecture has claimed promising results in [44] for air data sensors FD, and most recently in [45] for fault estimation. Despite the rapid developments of various DNN-based FD architectures, however, research efforts along the explainability and interpretability analysis line are still rare.

1.2.2. Interpretability analysis of DNN structures

DNN is commonly considered “black” for a long time. Why the DNN specifics are devised as such and how the enclosed operations work attract more and more attentions. To address such issue, we plan to explain the structure that corresponds to the DNN architecture specifics, and interpret the structure that depicts the operations enclosed in the DNN architecture. Similar works have appeared in literature.

The DNN structure corresponds to the specifics (e.g. CNN kernel size) that can be objectively optimized via certain metrics (e.g. DNN testing accuracy). To explain the large structure, comparative studies were commonly used. Different sets of parameters (number of CNN filters, kernel sizes, etc.) were assembled in the DNN and then the authors performed thorough training for each parameter set, finally decided the optimal one via gleaning the trained DNN[46]. Technical tools designed specifically for optimizing the DNN training were also found, of which the most peculiar one is the Microsoft’s NNI, which decides the best training coefficients (e.g. learning rate, iterative epochs) for a certain DNN architecture [47]. The Tree-structured Parzen Estimator (TPE) is a sequential model-based optimization (SMBO) approach, as a black-box optimization, which can be used in various scenarios and shows good performance.

Especially when limited by computation resources and can only try a small number of trials [48]. When an “optimal” DNN is found, ablation study is commonly used to verify the architecture (e.g. CNN branches, CNN-LSTM fusions), which involves cropping certain sub-architecture from the “optimal” one, and comparing the DNN performances. Typical examples are found in [14].

The DNN structure depicts the operations enclosed within the DNN (e.g. a certain CNN filter). It is usually analyzed via mirroring the DNN outputs to what humans understand in a certain context. For instance, in the visual object classification problem, CNN is commonly used. The understandable terms of humans in such a context are the visual features that one hinges on to classify an object (e.g. ‘ear’ or ‘nose’ of a cat/dog). Class activation mapping (CAM) thus was proposed in [15], and rapidly developed in [49, 50, 51, 52, 53, 54], which points out the highlighted region(s) wherein the CNN filters focus on. The CNN architecture may be considered reasonable (interpretable) if the highlighted region(s) corresponds to what humans tend to watch (e.g. the ‘ear’/‘nose’). Related studies in such line have made promising progresses which promoted both academic researches and industrial applications of CNN in vision-related problems—but “vision-related” only; very rare studies pertaining to such line was found in other DNN-based works (e.g. DNN-based fault detection).

1.2.3. Optimization methods of DNN

Once a prediction model is designed, it is ready to be optimized. Taking DNN as an example, a lot of factors (number of layers, kernel size, hyperparameters, etc.) may influence the performance of a DNN model. DNN model is designed and expected to be highly accurate, low delay and lightweight for real time prediction on edge devices, which are contradictory under certain circumstances. Therefore, it is important to clarify the application scenario and determine the goal and order of optimization.

Deep learning has been widely used because of its remarkable effect, but it is well known that deep neural network (DNN) has a great disadvantage that the amount of calculation is too large. More computing will directly lead to an

increase in cost. This shortcoming hinders the productization of deep learning methods, especially on some edge devices in aerospace engineering, which are not designed for computing intensive tasks. There will be many problems in power consumption and time delay if deep learning models are simply deployed. For the large-scale original model, it is the research focus that how to substantially simplify the model to reduce the amount of calculation and storage, which is called model compression and proposed as early as 1990 [55].

Model compression is a software method with low cost, which does not conflict and even can be added with the hardware acceleration method. The deep learning model can be compressed based on an assumption: over-parameterization of DNN, i.e. a large number of parameters of DNN are redundant and can be removed with little impact on the performance of DNN. The biggest advantage of model compression is the reduction of the computing time and power consumption. And it is more convenient to the deployment the DNN to edge devices or personal terminals when model size becomes smaller. There are many techniques of model compression, such as pruning, quantification, low rank decomposition, knowledge distillation, etc[56, 57, 58, 59, 60].

The hyperparameters have strong influences on the performance of deep learning model. Classifiers based on sophisticated feature extraction techniques have ten hyper-parameters or more, depending on how the experimenter chooses to parametrize the model, and how many hyper-parameters the experimenter chooses to fix at a reasonable default. Moreover, the evaluation of the fitness model is expensive when choose different combinations of hyperparameters. Consequently, optimization problem of hyperparameters could be difficult and time-consuming. Hyperparameter optimization is the problem of optimizing a loss function over a graph-structured configuration space[61]. There are also many algorithms to select the hyperparameters, which can be divided as model-free and model-based. For model-free methods, grid search[62] and random search[63] is typical representative, whose primary ideas can be inferred from their names. And the other model-based sounds more reasonable and convincing, including Bayesian optimization[64], evolutionary algorithms[65] and

other methods. Sequential Model-Based Global Optimization (SMBO) algorithms, which have been used in many applications where evaluation of the fitness function is expensive[66], will be adopted in this paper for model optimization.

1.3. Overview of this Paper

In this paper, exemplifying the FD problem of aircraft air data sensors, we aim to develop a DNN-based fault detection scheme with high accuracy and speed as well as lightweight so to deploy on the edge device. We highlight our work as:

- **Accurate and scalable FD performances:** We model the FD problem using aircraft IRU measurements as equivalent inputs; we also construct a dedicated dataset; via delicate architecture tuning, the DNN-based scheme claims accurate and scalable FD performances for different aircraft at various conditions.
- **Augmented Imagefication method for ADS data manipulation:** We propose the methodology in reshaping 1D data for the feature extraction and case prediction of DNN. The necessity of augmentation of ADS data and different kinds of augmented methods are discussed. The explainability of such methods specifics are studied based on Grad-CAM, which elevates the interpretability of how the DNN operations work.
- **Model optimization and online monitoring of flying condition based on edge device:** We adopt the model pruning and TPE-based hyperparameter finetuning to optimize the model for deployment on edge device. The online monitoring of flying condition is finally achieved, which provides a novel data-driven approach of fault detection on aircraft as well as and may bring inspiration to other engineering fields.

The remainder of this paper is organized as follows. Section 2 defines the problem. Section 3 illustrates the database. Section 4 proposes the imagefication method and experimental setup. Data augmentation in different ways are

detailed in Section 5. Section 6 studies the interpretability on augmented imagefication method based on Grad-CAM. In Section 7, pruning and TPE-based hyperparameter finetuning are implemented for model optimization, and online FD deployment on edge device is achieved. Finally conclusions and future works are discussed in Section 8.

2. Problem definition

To define the FD problem of aircraft air data sensors, we start with the air data evolution equations:

$$\begin{cases} \dot{V} = (A_x - gS_\theta)C_\alpha C_\beta + (A_y + gS_\phi C_\theta)S_\beta + (A_z + gC_\phi C_\theta)S_\alpha C_\beta \\ \dot{\alpha} = (-A_x S_\alpha + A_z C_\alpha + gC_\phi C_\theta C_\alpha + gS_\theta S_\alpha)/VC_\beta + w_y \\ \quad - (w_x C_\alpha + w_z S_\alpha)S_\beta/C_\beta \\ \dot{\beta} = [-(A_x - gS_\theta)C_\alpha S_\beta + (A_y + gS_\phi C_\theta)C_\beta - (A_z + gC_\phi C_\theta)S_\alpha S_\beta]/V \\ \quad + w_x S_\alpha - w_z C_\alpha \end{cases} \quad (1)$$

wherein S_* and C_* represent \sin and \cos operations, $\{V, \alpha, \beta\}$ are airspeed, AOA, and sideslip angle, g is the gravitational acceleration, $\{w_x, w_y, w_z\}$ and $\{\psi, \theta, \phi\}$ denote rotational speeds and angles, respectively. In Eq. (1), $\{A_x, A_y, A_z\}$ indicate the accelerations along different axes of the aircraft body, which are defined as $\{A_i = F_i/m\}_{i=x,y,z}$, wherein m is the mass of the aircraft, and $\{F_x, F_y, F_z\}$ are the external forces generated by the control actions:

$$\begin{cases} F_x = F_x(\delta_{th}, V, \alpha, S, \dots) \\ F_y = F_y(\delta_r, \delta_a, V, \alpha, S, b, c, \dots) \\ F_z = F_z(\delta_e, V, \alpha, S, c, \dots) \end{cases} \quad (2)$$

In Eq. (2), δ_* indicates individual control input (e.g. throttle δ_{th} , elevator δ_e , aileron δ_a , and rudder δ_r), S , c , and b are the aircraft wing area, mean chord length, and span, respectively.

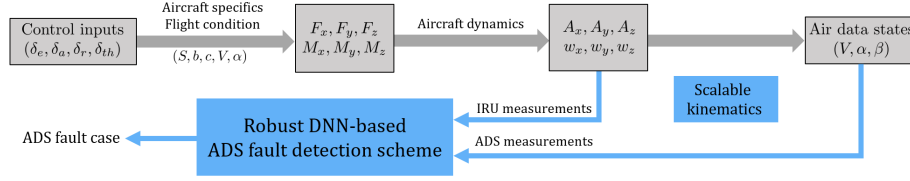


Figure 1: Aircraft motion equations and the fault detection scheme formulated in this paper.

The kinematics of aircraft rotational speeds and angles are written as:

$$\begin{cases} \dot{\psi} = w_y S_\phi / C_\theta + w_z C_\phi / C_\theta \\ \dot{\theta} = w_y C_\phi - w_z S_\phi \\ \dot{\phi} = w_x + w_y S_\phi S_\theta / C_\theta + w_z C_\phi S_\theta / C_\theta \end{cases} \quad (3)$$

and dynamics of the aircraft rotation yield:

$$\begin{cases} I_x \dot{w}_x - I_{xy} \dot{w}_y = M_x + (I_y - I_z) w_y w_z - I_{xy} w_x w_z \\ I_y \dot{w}_y - I_{xy} \dot{w}_x = M_y + (I_z - I_x) w_x w_z + I_{xy} w_y w_z \\ I_z \dot{w}_z = M_z + (I_x - I_y) w_x w_y + I_{xy} (w_z^2 - w_y^2) \end{cases} \quad (4)$$

wherein $\{M_x, M_y, M_z\}$ are the external control moments, which are defined as:

$$\begin{cases} M_x = M_x(\delta_a, \delta_r, V, \alpha, S, b, \dots) \\ M_y = M_y(\delta_a, \delta_r, V, \alpha, S, b, \dots) \\ M_z = M_z(\delta_e, V, \alpha, S, c, \dots) \end{cases} \quad (5)$$

Figure 1 depicts an overall flow for above equations. Traditional works hinge on model-based approaches to monitor the control inputs and sensors outputs. Implicitly in such model, the external control forces/moments must be considered, which are generated using associated control actions, and directly related to the aircraft specifics (e.g. wing area, mass) and flight conditions (e.g. airspeed, AOA). Parameters within such model-based FD scheme typically requires *ad hoc* tuning per aircraft/flight condition. Therefore, its scalability is doubtful.

Despite the high dependency of control forces/moments upon aircraft speci-

cs/flight conditions, their outcome (i.e. $\{A_i\}_{i=x,y,z}$ and $\{w_i\}_{i=x,y,z}$) can be directly measured using inertial reference unit (IRU). Via Eq. (3), rotational angles of the aircraft can also be calculated using $\{w_i\}_{i=x,y,z}$ (although dedicated sensors do exist to directly measure them). We thus adopt IRU measurements as a probe into the overall system, model them as equivalent inputs to the air data evolution, and perform the air data sensors FD task directly.

To be specific, the problem in this paper is defined as, to detect (classify) different faults that occur in the air data sensors, given the air data measurements $\{V, \alpha, \beta\}$, and other data resources which may include $\{A_x, A_y, A_z\}$, $\{w_x, w_y, w_z\}$, $\{\psi, \theta, \phi\}$ and $\{g_x, g_y, g_z\}$ (overload). The FD scheme is modeled as a mapping process (input: available data resources, output: fault case), which we aim to regress via deep neural networks.

3. Data preparation

3.1. Diverse aircraft and flight conditions

Data is essential for DNN training and validation. Most previous works discussed 1 aircraft only. In this paper, we allocate both simulation and real flight data from 5 different aircrafts which include 1 large cargo airplane (Y [67]), 2 passenger aircrafts (B₁ and B₂, [68, 69]), 1 general aviation (D [43, 44]), and 1 fighter aircraft (F [70]). We also involve 6 different flight conditions to cover the aircraft’s entire envelope, i.e. high, medium, and low altitudes for both cruise, manual free flight, and low-altitude landing/take-off cycle (LTO). Different control forms from both human pilot (manual) and automated control

Table 1: Different aircraft and flight conditions adopted in this paper.

Aircraft	General configuration	Weight	Span	Data source	Flight condition
Y	large cargo airplane, quadruple piston engines, high wing	41.0t	38.0m	simulation	• low altitude, LTO, manual
B ₁	large passenger aircraft, quadruple turbo engines, low wing	174t	59.6m	simulation	• high altitude, cruise, AP • low altitude, free flight, manual
B ₂	large passenger aircraft, double turbo engines, low wing	44.6t	35.8m	real flight	• low altitude, LTO, manual
D	general aviation, double piston engines, high wing	3.12t	19.8m	simulation	• high altitude, cruise, AP
F	fighter aircraft, double turbo engines, delta wing	10.5t	11.4m	real flight	• medium altitude, manual flight

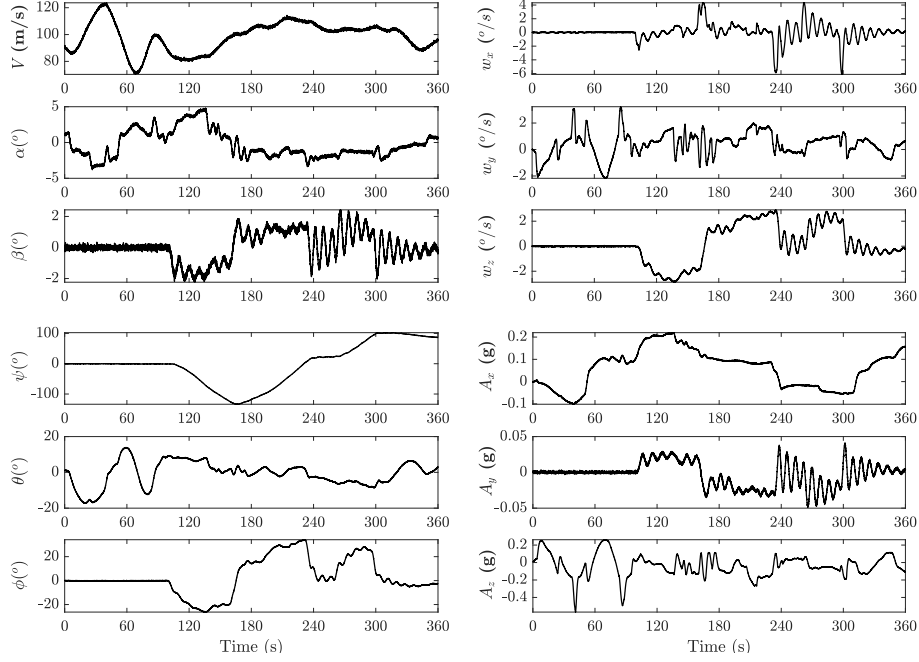


Figure 2: Plots of a sampled flight record allocated in our database.

laws (auto-pilot, AP) are also considered. See Table 1 for more details. In Figure 2 we also plot a sampled data we allocated in our database.

3.2. Measurement noises and disturbances

Both simulation and real flight data are considered in the paper. While measurement noises and disturbances exist naturally in the real flight, we adopt the model following [71] in simulation. Dryden atmospheric disturbances are injected to perturb the flight states, on which the measurement noises are added to generate the noise-corrupted data. Measurement noises are assumed to follow

Table 2: Measurement noise standard deviations in the simulation for aircraft D.

Sensor	Standard deviation	Unit
V_m	0.1	m/s
$\{\alpha, \beta\}_m$	$0.1\pi/180$	rad
$\{A_x, A_y, A_z\}_m$	0.01	m/s^2
$\{p, q, r\}_m$	$0.01\pi/180$	rad/s
$\{\psi, \theta, \phi\}_m$	$0.01\pi/180$	rad
$\{g_x, g_y, g_z\}_m$	0.01	—

Gaussian process distribution. Standard deviations for the noise of each sensor are characterized in Table 2 [16].

3.3. Designated training and testing

Training and testing data are strictly separated to avoid the over-fitting problem. We put all the real flight data in testing to fully evaluate the DNN performance. Diversity is crucial in specifying the training data, as the training algorithm is expected to extract from this data for an efficient FD mapping. We therefore adopt the real data from B₂, F, and simulated data from D, B₁ manual flight for testing. As for training, we use the data from Y manual LTO and B₁ AP cruise, see Table 3. In the table, an overview of the data for each aircraft/flight condition is also characterized using the minimum, maximum, and stand deviation of key (clean) flight states (i.e. altitude, airspeed, AOA, and sideslip angle).

3.4. ADS fault modeling and injection

Different sensor fault types have been discussed in previous works, which include ramp bias, oscillations, and drift. For airspeed, most flight accidents happened due to the Pitot tube being clogged by ice/rain. We thus consider drift fault for airspeed (measurement loss). For AOA and sideslip angles, the deflection vanes may be stuck or perturbed by external atmosphere, which causes drift (constant bias) and extra noises. As in Table 4, a total of 5 ADS fault cases are discussed in this paper, wherein the magnitude for each case is specified following [44].

We implement the ADS faults in an additive form; i.e., the “clean” data (Case 0 in Table 4) are retrieved from real flight/simulation. Sensor faults are

Table 3: Training and testing data specifics in this paper.

	Aircraft & Condition	Duration (min)	Altitude (km)	Airspeed (m/s)	AOA (°)	Sideslip angle (°)	Cases distribution in {0~5} (%)
Training	B ₁ AP cruise	327	[9.63, 10.7, 0.35]	[227, 252, 9]	[-1.3, 0.6, 0.4]	[-1.9, 0.4, 0.6]	{27, 13, 16, 16, 14, 14}
	Y manual LTO	295	[0.03, 0.66, 0.11]	[93, 167, 14]	[-2.7, 7.7, 1.2]	[-2.2, 1.6, 0.3]	{28, 14, 13, 13, 18, 14}
	B ₂ manual LTO	67	—	[75, 151, 12]	[0.8, 6.7, 0.8]	[-1.5, 0.5, 0.3]	{28, 20, 14, 11, 16, 11}
Testing	F manual flight	30	—	[80, 141, 21]	[10, 46, 11]	[-3.8, 9.6, 2.5]	{10, 10, 17, 19, 15, 29}
	D AP cruise	162	[3.50, 4.00, 0.19]	[68, 71, 0.38]	[0.5, 3.2, 0.37]	[-7.3, 2.7, 2.2]	{23, 16, 17, 14, 17, 13}
	B ₁ manual flight	151	[0.01, 1.61, 0.26]	[47, 276, 31]	[-14, 19, 4]	[-8, 5, 1]	{29, 16, 11, 14, 14, 16}

Note: [minimum, maximum, stand deviation] of clean altitude and ADS states are characterized; altitude was not recorded in B₂ and F real flight.

Table 4: ADS fault cases adopted in this paper.

Case	Sensor	Fault type	Magnitude*
5	sideslip angle	extra noise	$5^\circ \sim 10^\circ$
4	sideslip angle	drift	$\pm(5^\circ \sim 10^\circ)$
3	AOA	extra noise	$5^\circ \sim 10^\circ$
2	AOA	drift	$\pm(5^\circ \sim 10^\circ)$
1	airspeed	drift	$-(50\% \sim 100\%)$
0	clean measurement with noises and disturbances, no fault		

* Noise standard deviation and drift values defined in this column.

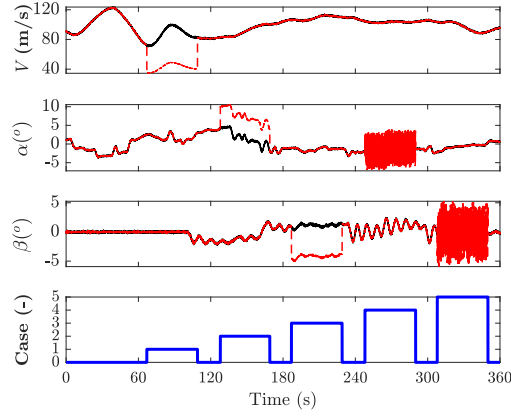


Figure 3: Illustrative plot for the fault injection. Black lines denote clean states from real flight/simulation, red the fault-injected data. The FD scheme is expected to detect the different fault cases (blue thick line) based on available data measurements and proper DNN operations.

then injected into the ADS data. Following [44], this injection is performed in a randomized manner; i.e., for every 60 seconds in the data, the fault cases occur randomly at randomized moments, with its duration (also randomized) not exceeding the 60 seconds. In Figure 3, different fault cases are injected to both airspeed, AOA, and sideslip angle for illustrative purposes. Table 3 also presents the distribution of different cases in the final data we adopt for the DNN training/testing.

4. Imagefication method for ADS fault detection

4.1. Data-driven method for ADS fault detection

Deep neural networks are proven a very effective way for image classification problems. Our previous works advocated a fusion of CNN and LSTM in designing the DNN architecture [43, 44] for parameter identification, icing detection, etc. In our recent study in fault diagnosis of Inertial Measurement Unit (IMU) sensors, a novel data driven method, CNN-LSTM-fusion architecture is used for fault classification[72].

In CNN [73], convolutional filters scan the input (e.g. an image), of which the results are concatenated as feature maps. Multiple filters yield various feature maps, which being stacked to construct the designated mapping. Activation functions and pooling operations may also be used, with the former adding to nonlinearity in the mapping, and the latter the noise-tolerance [43, 44, 74].

LSTM is typically used for sequential data. Different from the spatial local-connectivity features extraction in CNN, it aims to abstract the temporal knowledge. Previous DNN including RNN [73] also targets the temporal features. RNN, however, may suffer error explosion/vanishing problems in the training. LSTM adopts gate operations to automatically select the historic input that may be useful in the mapping. As proved in many works, training efficiency, mapping accuracy, and deployment cost of LSTM can all be improved [43, 44].

It can be inferred that the deep neural networks also work for ADS fault detection problems. In coping with the dynamics problem, both CNN and LSTM may be useful. However, combination causes complexity. We want to find a simple way, if satisfactory enough, to model the fault detection problem. Therefore, The CNN is chosen to handle the problem. As there is not an input explicitly defined as “image”, the key in implementing CNN in these problems is to reshape the dynamics data (e.g. flight states, control commands) into an image-like format, i.e., *Imagefication*, which is elaborated in section 4.2.

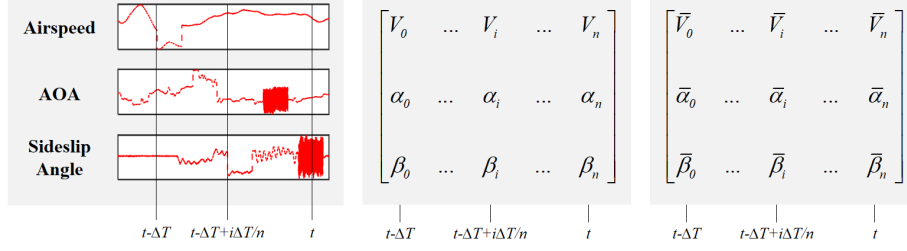


Figure 4: Data imagefication for ADS. Left: ADS records (V , α , β) are retrieved from real flight/simulation, faults are injected into the records; a time window (ΔT) is implemented to clip the data, which is further down-sampled to $1Hz$. Middle: the clipped and down-sampled data are stacked as the matrix. Right: along each row, the states are normalized linearly within the range of $[0, 1]$. Same approaches are also used for accelerations, rotational speeds, etc., which eventually yields a 15×31 state image for the ADS data.

4.2. Imagefication manipulation

Imagefication is a data manipulation process for 1 dimensional data (vector), such as ADS data from different channels, to generate the image-formatted data (matrix), so it can be treated as standard input to CNN. Take an example of V , α , β , as shown in Figure 4. Via real flight or simulation, we have the records of different states. We inject faults into the ADS states, allocate all other flight data, and stack them into a 2D matrix (middle plot). In this matrix, each row stands for the historic measurements of a certain state, and column the value of that state at a certain moment. For each group of the aircraft flight state (e.g. air data, accelerations, rotational speed, and rotational angles), we stack this matrix separately.

Time window is also used. At each moment t , we consider the flight records in a range from previous $t - \Delta T$ to t (both included), wherein ΔT is $30s$ ¹. For different aircraft, the data is recorded in various sampling rates (e.g. $20Hz$ for B_1 , $30Hz$ for F). We down-sample them to a unified frequency at $f_s = 1/\Delta t$, wherein $\Delta t = \Delta T/n = \Delta T/30 = 1s$. We then stack the state matrix using the re-sampled data.

¹Following [43, 44], this window may be understood as a compromise between the aircraft “fast” motion modes of which the periods are in seconds (e.g. longitudinal short period, lateral roll), and “slow” modes which typically last for tens/hundreds of seconds (e.g. longitudinal phugoid, Dutch roll).

In the down-sampled flight data, the range of each state varies significantly (see Table 3). In practice, this may create numerical difficulties in the DNN training (singularities, error vanishing/explosion). Normalization is adopted to process the sampled data. Following [43, 44], this normalization is performed linearly along each row of the stacked matrix. After normalization, the “image” we obtain in the right plot of Figure 4 is adopted as input to the CNN.

5. Data augmentation methods and comparison

5.1. necessity of ADS data augmentation

After imagefication manipulation shown in Figure 4, the data of airspeed, angle of Attack, slideslip angle, accelerations, rotational speeds acquired from ADS (shown in Table 2) are constructed like grayscale images. Each image has the 2D matrix shape 15×31 . In previous studies[72], a new deep neural network for fault detection is established, because this image shape is not commonly seen in image processing studies.

On the one hand, we find that the feature maps are becoming vectors (1 D data) after several convolutional layers because of the quantity difference in different dimensions of the image matrix. It is inevitable when we set one dimension as the physical parameters ($V, \alpha, \beta, A_x, A_y, A_z, p, q, r, \psi, \theta, \phi, g_x, g_y, g_z$) and the other as the sampling data of ADS. The more data we sample from ADS, the longer and narrower the matrix shape is. Consequently, the convolutional kernels (mostly 3×3 size) are not well functioned for extracting the feature of the data when performing the convolutional manipulation for 1 D vector. The considerable connection between different physical parameters may be easily missed because of the first convolution at the beginning. In other words, the convolutional kernel is too large for the dimension of physical parameters. Even the smallest kernel size 2×2 is chosen (1×1 convolution completely ignores the relationship with surrounding data), it is still too large and it is preposterous to chose a fraction as kernel size, such as 1.1×1.1 , 1.2×1.2 , etc. Therefore, almost the only strategy is augmenting the image matrix data to fully utilize the

convolutional manipulation. On the other hand, there are many mature CNN models that have been proven to be effective, such as VGG net[75], ResNet[76] and so on. The input image size of these models is typically 224×224 . It is more natural and easier to adopt the existing mature model than develop and test a new deep neural network with different structures. For these reasons, it is a necessary and logical way to augment the image-like data to typical size (224×224) for modeling the fault detection network.

5.2. Experimental Setup

In training/testing the DNN, we record both training loss and validation accuracy (with all testing data designated as the validation dataset). Following [44], we repeatably perform 30 training runs for all DNN architectures, excluding the best/worst 5 runs, and summarize the outcome via the remained 20 records. We also adopt Pytorch 1.10 as backend and python version 3.8 in the programming. Our computational platform is configured with CUDA 11.3 (GPU: Nvidia RTX3090) in Windows 10 system . The platform has one i9-9900K CPU and 64GB RAM.

5.3. Comparison of different data augmentation methods

There are so many data augmentation ways: flip, rotation, scale, shear, translation, interpolation and even Generative Adversarial Networks (GANs)[77] designed mainly to avoid overfitting of networks, which is some different from reconstructing the matrix shape in this paper, that is, to transfer the original shape of matrix from 15×31 to 224×224 . Taking the dimension of ADS signal along with time as example, if we interpolate the points from 31 to 224, the fault with the type of sudden change (jump) will turn into a slowly rise or fall, which may hinder the feature extraction of convolution layer in CNN. Here we propose a data augmentation method called “duplication”, considering the existing flip method, the different combinations of these methods are discussed.

The scheme of data “duplication” is shown in Figure 5. Notice that the shape of imagefication matrix is 15×31 (upper left corner of the figure), then

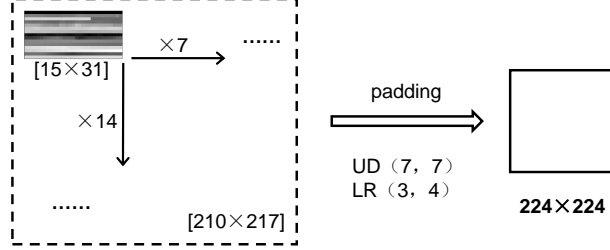


Figure 5: Augmentation scheme for ADS imagefication data.

we duplicate the data of each dimension until the shape of matrix is closest to 224×224 , so the data from different views of dimensions are duplicated 7 and 14 times, respectively. Thus, a matrix shaped 210×217 can be obtained. Finally, the zero-padding operation is implemented for rounding up the shape. The edges of matrix, i.e., the up, down, left and right edges of the image are filled with 7, 7, 3 and 4 lines of zeros. In this way, a image with the shape of 224×224 for CNN model is constructed.

The key point of data augmentation in Figure 5 is how to duplicate the original matrix to 14×7 times. There are many kinds of methods and their combinations are also needed to be discussed. Let the imagefication matrix write as $M_{(m \times n)}$ with dimensions $m = 15$ and $n = 31$, respectively. And $a \times b$ is the duplication multiple of dimensions.

Flip is a typical transformation for a matrix. P with shape $n \times n$ in Equation 7 is an anti-diagonal identity matrix whose all counter-diagonal elements are 1 and other elements are 0. Then we have

$$M_{lr} = MP \quad (6)$$

Where M_{lr} is the left-right flip of the matrix M . Similarly, the up-down flip M_{ud} can be performed by multiplying the anti-diagonal identity matrix in the

other dimension.

$$P = \begin{pmatrix} 0 & 0 & \dots & 0 & 1 \\ 0 & 0 & \dots & 1 & 0 \\ \vdots & \vdots & \ddots & \vdots & \vdots \\ 0 & 1 & \dots & 0 & 0 \\ 1 & 0 & \dots & 0 & 0 \end{pmatrix} \quad (7)$$

There are two kinds of methods when copy the original matrix. One is called “repeat”, the other is “tile”. Repeat operation is from the perspective of elements x_{ij} , which broadcast from 1×1 to $a \times b$, as shown in Equation 8. Tiling operation is repeating the whole matrix $a \times b$ times in respective axes, seen in Equation 9. Therefore, the different three data augmentation methods and their combinations should be studied and compared, as shown in Figure 6.

$$M_{repeat} = \begin{bmatrix} \overbrace{\begin{matrix} x_{11} & x_{11} & x_{11} \\ x_{11} & x_{11} & x_{11} & \dots & \dots \\ x_{11} & x_{11} & x_{11} \end{matrix}}^{(a \times b)} & & \\ & \ddots & \ddots & & \vdots \\ & & & \overbrace{\begin{matrix} x_{mn} & x_{mn} & x_{mn} \\ x_{mn} & x_{mn} & x_{mn} \\ x_{mn} & x_{mn} & x_{mn} \end{matrix}}^{(a \times b)} & & \end{bmatrix} \quad (8)$$

$$M_{tile} = \begin{bmatrix} \overbrace{\begin{matrix} M & \dots & M \\ \vdots & \ddots & \vdots \\ M & \dots & M \end{matrix}}^{(a \times b)} \end{bmatrix} \quad (9)$$

Table 5 specifically explained the different data augmentation methods of Figure 6. In All_Flip, All_Repeat and All_tile augmentations, the same operation is implemented in two axes of the original matrix. The other 4 augmentation

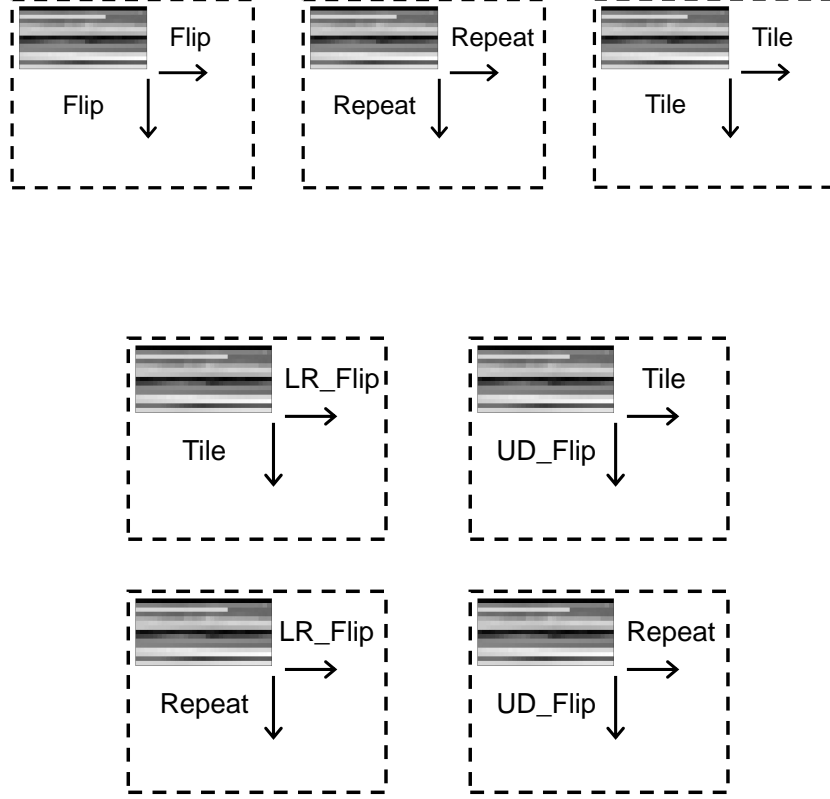


Figure 6: Different data augmentation methods.

methods are the combinations between flipping with repeat or tiling. When the matrix is flipped along one axis, it then will be tiled the whole data or repeated the elements along the other axis.

The deep neural network that we choose for fault detection is VGG-16[75]. VGG-16 is a preferred model with excellent generalization performance in deep learning, whose architecture is shown in Figure 7. The input channel is reset to 1 since the augmented grayscale image is a 2D matrix. And the output number of the final soft-max layer is set to 6, the number of fault types. The training and testing are implemented with all augmentation methods under the

Table 5: Different data augmentation operation.

Number	Name	Operation
1	All_Flip	M and M_{lr} M_{ud} are alternatively arranged in each axis respectively
2	All_Repeat	Repeat all elements from 1×1 to $a \times b$
3	All_Tile	Tile the whole matrix M in all axes
4	LR_Flip & Tile	M and M_{lr} are alternatively arranged in rows and M is tiled in columns
5	UD_Flip & Tile	M and M_{ud} are alternatively arranged in columns and M is tiled in rows
6	LR_Flip & Repeat	M and M_{lr} are alternatively arranged in rows and elements of M is repeated in columns
7	UD_Flip & Repeat	M and M_{ud} are alternatively arranged in columns and elements of M is repeated in rows

same network VGG-16 with the same hyperparameters. In detail, epoch 500, learning rate 0.0001, batch size 100 and momentum 0.9.

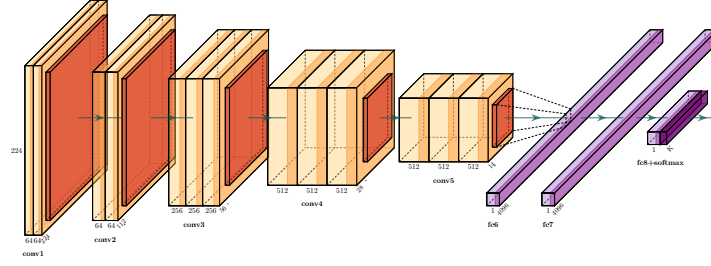


Figure 7: VGG-16 architecture.

The test accuracies every 5 epochs of networks with different augmentation methods are shown in Figure 8. It is satisfactory that all fault detection models with different augmentation methods converge after no more than 100 epochs, and the all the test accuracies are higher than 90%, which proves the effectiveness of the data augmentation method we proposed. Comparing these methods, many interesting useful conclusions can be drawn.

Firstly, comparing the same operations in two axes (operation No.1-3), it is obvious that the model with All.Repeat operation is the best with the highest accuracy, and the second is All.Flip, the last is All.Tile. Secondly, comparing

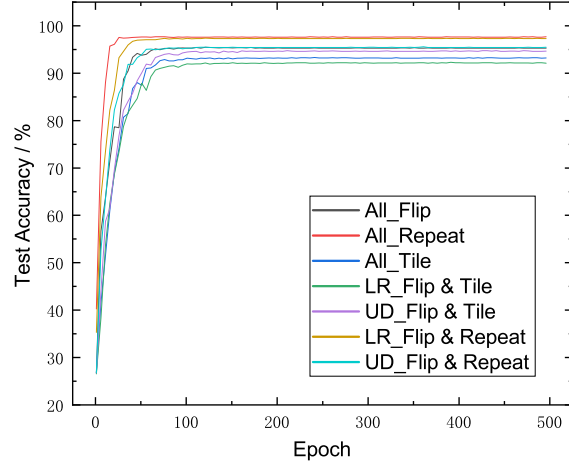


Figure 8: Training performances of different augmentation methods.

the Repeat and Tile operations (operation No.2 and 3, 4 and 6, 5 and 7), it can be concluded that Repeat operation yields higher accuracies than Tile operation. Thirdly, comparing the Flip and Tile operations (operation No.1, 3-5), it is obvious that Flip operation leads to higher accuracy than Tile operation, whether LR_Flip or UD_Flip.

However, comparing the LR_Flip and UD_Flip operations, the conclusion becomes more complicated. The LR_Flip operation leads to lower accuracy than UD_Flip under the Tile operation in the other axis (operation No.4 and 5), on the contrary, the higher accuracy than UD_Flip with Repeat operation in the other axis (operation No.6 and 7). So it can be summarized that the LR_Flip and UD_Flip operations are coupled with the Tile and Repeat operations, of which combination is responsible for the performance of the fault detection network.

The best training accuracies and test accuracies are detailed in Table 6. It is clear that the Repeat operation yields the higher accuracies, as revealed by operation No.2, 6 and 7. All_Repeat lead to the best train and test accuracies (100% and 97.704%), LR_Flip & Tile results in the lowest accuracy (98.898% in

train set and 92.296% in test set).

Table 6: Best accuracies of different data augmentation operation.

Number	Operation	Train accuracy /%	Test accuracy /%
1	All_Flip	99.963	95.481
2	All_Repeat	100	97.704
3	All_Tile	99.611	93.370
4	LR_Flip & Tile	98.898	92.296
5	UD_Flip & Tile	99.061	94.741
6	LR_Flip & Repeat	100	97.407
7	UD_Flip & Repeat	99.996	95.556

Overall the All_Repeat operation leads to the highest accuracy (100% in train set and 97.704% in test set) and the fastest convergence speed among all methods, which indicates that the operation of repeating the elements is the most effective way of augmentation for ADS data. In next studies, the Repeat operation is determined as the data augmentation method.

6. Interpretability analysis on augmented imagefication method

Neural networks were considered as a “black box” for a long time. Why does the VGG-16 with All_Repeat data augmentation method work so well for fault detection? As shown in Figure 9, flight records corresponding to fault Case 4 (Table 4, sideslip angle drift) are plotted. The width of the image corresponds to the time window (30s), and the 15 rows (from top to bottom) indicates normalized $V, \alpha, \beta, A_x, A_y, A_z, p, q, r, \psi, \theta, \phi$, respectively. The sideslip drift fault is marked with a red box. Figure 10 depicts the imagefication visualization before and after augmentation for the records in Figure 9 (Note: the lines of borders in augmented image do not actually exists, just for visualization convenience of zero-padding in edges). It can be explained that the Repeat elements operation enlarges the fault characteristics so the ADS data with fault can be detected by convolutional neural networks. We want to explore the interpretability of the air data convolutional operations in VGG-16, as it affects the performance most significantly.

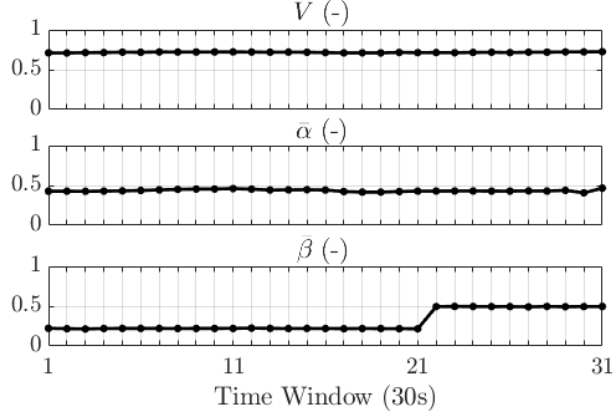


Figure 9: Normalized flight records for features visualization; as in Figure 4, the data has been downsampled to $1Hz$; the sideslip drift fault occurs at last 1/3 of the window, i.e 21~31s.

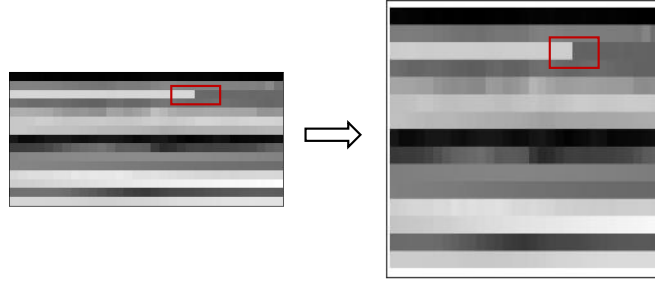


Figure 10: Typical fault (β drift) in original and augmented imagefication.

It is undoubted that we must build ‘transparent’ models that have the ability to explain why they predict what they predict. To better illustrate the features-extraction of VGG-16, we adopt the Gradient-weighted Class Activation Mapping (Grad-CAM) technique[54], which is a generalization of Class Activation Mapping (CAM). Suppose Grad-CAM $L_{\text{Grad-CAM}}^c \in \mathbb{R}^{u \times v}$ with width u and height v for any class c , $\frac{\partial y^c}{\partial A^k}$ is the gradient of the score for class c , y^c with respect to feature map activations A^k of a convolutional layer. These gradients flowing back are global-average-pooled 2 over the width and height dimensions

(indexed by i and j respectively) to obtain the neuron importance weights α_k^c :

$$\alpha_k^c = \frac{1}{Z} \overbrace{\sum_i \sum_j}^{\text{global average pooling}} \underbrace{\frac{\partial y^c}{\partial A_{ij}^k}}_{\text{gradients via backprop}} \quad (10)$$

Where Z is the number of pixels in the feature map ($Z = \sum_i \sum_j 1$). The weight α_k^c represents a partial linearization of the deep network downstream from A , and captures the ‘importance’ of feature map k for a target class c . Finally, the Grad-CAM can be obtained by a sequential processing of linear combination (weighted combination of forward activation maps) and a nonlinear operation (ReLU function):

$$L_{\text{Grad-CAM}}^c = \text{ReLU} \left(\underbrace{\sum_k \alpha_k^c A^k}_{\text{linear combination}} \right) \quad (11)$$

Figure 11 is the visualization of the Grad-CAM plots for the case 4 in Figure 10. Note a “hotter” mapping on CAM indicates the highlighted regions that convolution hinges on to assert the FD output. In Figures 11, Grad-CAM corresponds to a more general and abstract understanding of the FD problem, as the highlighted hotter (red) regions overlap the areas that the fault occurs (marked by red rectangles). It is also noticed that there are some hot areas in the junctions between different physical parameters, which may indicate that some combinations of these parameters also contribute to the FD case prediction.

7. Model optimization for mobile hardware deployment

7.1. Model compression method-Pruning

7.1.1. Model pruning theories

In this paper, a pruning method is introduced[78] for VGG-16 compression. Based on the assumption that parameters of DNN are independent, the main

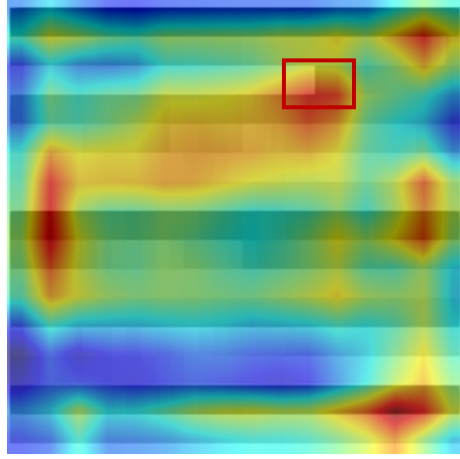


Figure 11: Illustrative Grad-CAM plots for Fault case 4 in 10; the highlighted (red hot) features correspond to the faults occurred on the imagefication data (marked with red boxes).

idea of pruning method is solving a combinatorial optimization problem:

$$\begin{aligned} \min_{\mathcal{W}'} \Delta \mathcal{C}(h_i) &= \left| \mathcal{C}(\mathcal{D} \mid \mathcal{W}') - \mathcal{C}(\mathcal{D} \mid \mathcal{W}) \right| \\ &= \left| \mathcal{C}(\mathcal{D}, h_i = 0) - \mathcal{C}(\mathcal{D}, h_i) \right| \quad \text{s.t.} \quad \|\mathcal{W}'\|_0 \leq B \end{aligned} \quad (12)$$

Where h_i is the output produced from parameter i , $h = \{z_0^{(1)}, z_0^{(2)}, \dots, z_L^{(c_l)}\}$. \mathcal{D} is the set of training examples $\{\mathcal{X} = \{x_0, \dots, x_N\}, \mathcal{Y} = \{y_1, \dots, y_N\}\}$, x and y represent an input and a target output, respectively. \mathcal{W} is the parameters of DNN, $\left\{(\mathbf{w}_1^1, b_1^1), \dots, (\mathbf{w}_L^{C_\ell}, b_L^{C_\ell})\right\}$, which are to be optimized to minimize a cost value $\mathcal{C}(\mathcal{D} \mid \mathcal{W})$. $\mathcal{W}' = \mathbf{g}\mathcal{W}$, \mathbf{g} is vectorized pruning gate $\mathbf{g} \in \{0, 1\}^{C_l}$. $\mathcal{C}(\mathcal{D}, h_i = 0)$ is a cost value if output h_i is pruned, while $\mathcal{C}(\mathcal{D}, h_i)$ is the cost if it is not pruned. the l_0 norm in $\|\mathcal{W}'\|_0 \leq B$ bounds the number of non-zero parameters B in \mathcal{W}' . Equation 12 points out that we refine a subset of parameters that preserves the accuracy of the adapted network when pruning. The criteria for pruning is Taylor expansion. Approximating $\mathcal{C}(\mathcal{D}, h_i = 0)$ with a first-order Taylor polynomial near $h_i = 0$, we have

$$\mathcal{C}(\mathcal{D}, h_i = 0) = \mathcal{C}(\mathcal{D}, h_i) - \frac{\delta \mathcal{C}}{\delta h_i} h_i + R_1(h_i = 0) \quad (13)$$

where $R_1(x)$ is the first-order remainder and can be neglected due to the significant calculation required as well as a smaller second order term deduced from the widely-used ReLU activation function. Ignoring the remainder, we have $\Theta_{TE} : \mathbb{R}^{H_l \times W_l \times C_l} \rightarrow \mathbb{R}^+$, with

$$\Theta_{TE}(h_i) = |\Delta \mathcal{C}(h_i)| = \left| \mathcal{C}(\mathcal{D}, h_i) - \frac{\delta \mathcal{C}}{\delta h_i} h_i - \mathcal{C}(\mathcal{D}, h_i) \right| = \left| \frac{\delta \mathcal{C}}{\delta h_i} h_i \right| \quad (14)$$

Θ_{TE} is computed for a multi-variate output, such as a feature map, by

$$\Theta_{TE}(z_l^{(k)}) = \left| \frac{1}{M} \sum_m \frac{\delta \mathcal{C}}{\delta z_{l,m}^{(k)}} z_{l,m}^{(k)} \right| \quad (15)$$

where M is length of vectorized feature map.

7.1.2. Pruning result of VGG-16

Based on the above technique, the VGG-16 model with highest accuracy by All_Repeat data augmentation method in Section 5.3 is to be pruned. The performance indexes of pruning that we concern are best test accuracy, number of parameters, size of model, and time delay of evaluating. Time delay is the average time of making a prediction from input data to output case and can be calculated by $T = T_{total}/M$, where T_{total} is the time cost of evaluating all the input data, M is the number of all samples.



Figure 12: NVIDIA Jetson Nano[79] for DNN deployment.

The hardware platform we choose to be deployed in this paper is an edge device, NVIDIA Jetson Nano[79], as shown in Figure 12. It is a powerful, small and easy to use computer with low power consumption for image classification, object detection, speech processing, etc. The VGG-16 model is pruned and retrained with the same hyperparameters on Jetson Nano and the results are shown in Table 7. The relative change is calculated by $|(After - Before)/Before|$. It is obvious that the pruning result is satisfying. The best test accuracy is slightly up by 0.27%, the number of parameters is significantly reduced by 98.79% and the model size is 98.79% smaller than original VGG-16. Time delay is reduced by 87.54%, which means the recognition speed of pruned model is more than 8 times as quick as original model. In general, the pruned model with high accuracy and low time delay is very suitable for deployment on the edge device.

Table 7: Comparison between before and after pruning of VGG-16.

	Accuracy	Parameters No.	Size/Mb	Time delay/ms
Before	97.704%	134283974	524.56	297
After	97.963%	1624003	5.96	37
Relative Change	0.27% \uparrow	98.79% \downarrow	98.86% \downarrow	87.54% \downarrow

7.2. hyperparameter optimization base on Tree-structured Parzen Estimator (TPE) approach

7.2.1. Tree-structured Parzen Estimator approach

In an application where the true fitness function $\mathcal{X} \rightarrow \mathbb{R}$ is costly to evaluate, model-based algorithms approximate f with a surrogate that is cheaper to

evaluate. The algorithm is shown in Function 16.

$$\begin{array}{ll}
\text{SMBO}(f, M_0, T, S) & \\
1 \quad \mathcal{H} \leftarrow \emptyset & \\
2 \quad \text{For } t \leftarrow 1 \text{ to } T & \\
3 \quad x^* \leftarrow \operatorname{argmin}_x S(x, M_{t-1}) & \\
4 \quad \text{Evaluate } f(x^*) \quad \triangle \text{ Expensive step} & (16) \\
5 \quad \mathcal{H} \leftarrow \mathcal{H} \cup (x^*, f(x^*)) & \\
6 \quad \text{Fit a new model } M_t \text{ to } \mathcal{H} & \\
7 \quad \text{return } \mathcal{H} &
\end{array}$$

where x^* is the point that maximizes the surrogate (or its transformation), f is the true function that should be evaluated via observation history \mathcal{H} . The algorithms in this work optimize the criterion of Expected Improvement (EI) [80]. Expected improvement is the expectation under some model M of $f : \mathcal{X} \rightarrow \mathbb{R}^N$ that $f(x)$ will exceed (negatively) some threshold y^* :

$$\text{EI}_{y^*}(x) := \int_{-\infty}^{\infty} \max(y^* - y, 0) p_M(y|x) dy \quad (17)$$

The tree-structured Parzen estimator (TPE) [81] deviates from the standard SMBO algorithm in that it creates two hierarchical processes, $l(x)$ and $g(x)$ acting as generative models for all domain variables, which are defined as follows:

$$p(x|y) = \begin{cases} \ell(x) & \text{if } y < y^* \\ g(x) & \text{if } y \geq y^* \end{cases} \quad (18)$$

where $l(x)$ is the density formed by using the observations $\{x^{(i)}\}$ such that corresponding loss $f(x^{(i)})$ was less than y^* . $g(x)$ is the density formed by using the remaining observations.

According to the Bayes formula, the EI can be written as:

$$\begin{aligned} EI_{y^*}(x) &= \int_{-\infty}^{y^*} (y^* - y) p(y|x) dy \\ &= \int_{-\infty}^{y^*} (y^* - y) \frac{p(x|y)p(y)}{p(x)} dy \end{aligned} \quad (19)$$

By construction, $\gamma = p(y < y^*)$, and $p(x) = \int_{\mathbb{R}} p(x|y)p(y)dy = \gamma\ell(x) + (1 - \gamma)g(x)$, so we have

$$\begin{aligned} &\int_{-\infty}^{y^*} (y^* - y) p(x|y)p(y)dy \\ &= \ell(x) \int_{-\infty}^{y^*} (y^* - y) p(y)dy \\ &= \gamma y^* \ell(x) - \ell(x) \int_{-\infty}^{y^*} p(y)dy \end{aligned} \quad (20)$$

Finally,

$$\begin{aligned} EI_{y^*}(x) &= \frac{\gamma y^* \ell(x) - \ell(x) \int_{-\infty}^{y^*} p(y)dy}{\gamma\ell(x) + (1 - \gamma)g(x)} \\ &\propto \left(\gamma + \frac{g(x)}{\ell(x)}(1 - \gamma) \right)^{-1} \end{aligned} \quad (21)$$

Therefore, to maximize improvement the points x is supposed to be with high probability under $\ell(x)$ and low probability under $g(x)$. On each iteration, the TPE algorithm returns the candidate x^* with the greatest EI.

7.2.2. Hyperparameters optimization of DNN based on TPE

To further improve the performance of deep learning model in deployment, the pruned VGG-16 model in section 7.1.2 is chosed for the next optimization. The learning rate, number of epochs and batch size are selected to be optimized and the optimization target is the accuracy of predictions. the value of learning rate is a choice of $\{0.001, 0.0001, 0.00001\}$, the value of number of epochs is a choice of $\{1000, 800, 600\}$, the value of batch size is a choice of $\{120, 100, 80\}$. Considering that the optimization of different combinations of hyperparameters

could be time-consuming, the total number of trails is set as 10.

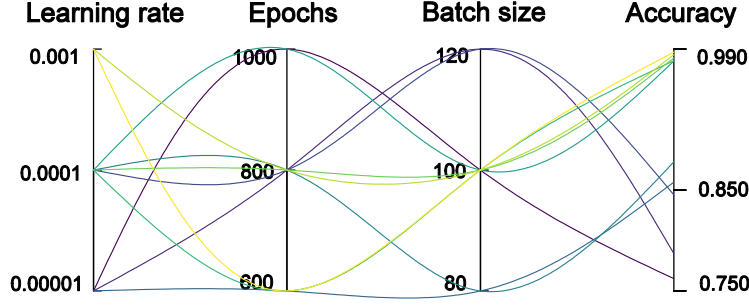


Figure 13: Optimization results of hyperparameters based on TPE.

The toolbox NNI developed by Microsoft [47] for optimization is adopted. Given different DNN architectures, NNI probes into the architecture, analyzes the training data, and decides an optimal combination of the training parameters. Different DNN architectures are trained separately in associated “optimal” ways, which we believe provides more solid ground for comparative studies. After training and optimization running process, different combinations of learning rate, epochs, and batch size are examined, the results are acquired and shown in Figure 13. It can be concluded that not one single hyperparameter, but the coupling effect of these hyperparameters influence the performance of DNN. The combination of learning rate 0.001, iterative epochs 600, and batch size 100 yields the optimal DNN training outcome, i.e., highest accuracy at 0.987.

7.3. Online fault detection deployment

Based on above optimization processes, a lightweight fault detection DNN model with high performance is obtained and can be very fit for online deployment. Just as we originally envisaged, an online fault detection deployment based on edge device is designed and developed. The online fault detection scheme is shown in Figure 14, where the different kinds of ADS data (normal

and fault) are simulated on PC and transmitted to Jetson Nano for online processing. The PC and Jetson Nano are connected via WiFi in local area network (LAN), and the User Datagram Protocol (UDP) is choosed for data transmission because of its simplicity, resource saving and high speed. Then the ADS data pass through augmented imagefication module and feed into optimal FD model. Finally, the prediction of flying condition can be made and hence the real time monitoring of aircraft is achieved.

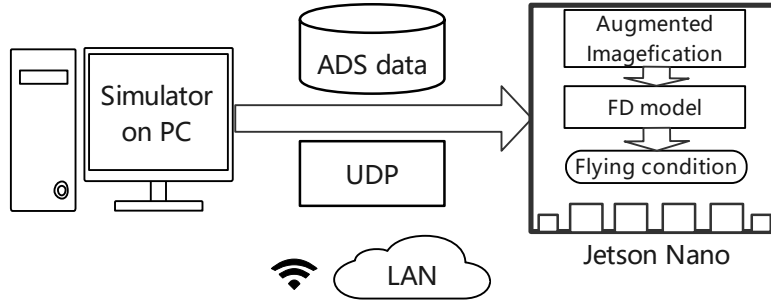


Figure 14: Online fault detection scheme.

8. Conclusion and Future Works

Exemplifying the fault detection (FD) problem of aircraft air data sensors, a augmented imagefication method DNN-based FD scheme is proposed in this paper.

- The FD problem is modeled using aircraft inertial referent unit measurements as equivalent inputs, and a dedicated database is constructed which involves different aircrafts/conditions, providing a solid basis in training/testing the DNN.
- An ADS data reconstructing method named Augmented Imagefication is proposed for the DNN-based prediction of flying conditions. The raw

data are reshaped as a grayscale image for convolutional operation, and the necessity of augmentation is analyzed and pointed out. Different kinds of augmented method, i.e. Flip, Repeat, Tile and their combinations are developed and compared, the result shows that the All_Repeat operation in both axes of image matrix leads to the best performance of DNN.

- The interpretability of DNN is studied based on Grad-CAM, as the highlighted hotter (red) regions overlap the areas that the fault occurs, which corresponds to a more general and abstract understanding of how DNN works the FD problem out.
- The DNN model, VGG-16 with augmented imagefication data is optimized for mobile hardware deployment. After pruning of DNN, the best test accuracy is slightly up by 0.27%, the number of parameters is significantly reduced by 98.79%, the model size is 98.79% smaller than original VGG-16 and time delay is reduced by 87.54%, which shows that the pruned model with high accuracy and low time delay is very suitable for deployment on the edge device. Then the hyperparameters optimization of DNN based on TPE is implemented and the best combination of hyperparameters is obtained, that is, learning rate 0.001, iterative epochs 600, and batch size 100 yields the highest accuracy at 0.987. Finally, an online FD deployment based on edge device, Jetson Nano, is developed and the real time monitoring of aircraft is achieved.

As a continuation of the work in this paper, it is promising to implement similar augmented imagefication method to other FD problems, e.g. aircraft actuators faults, communication datalink failures in commercial airlines. Moreover, interpretation of other DNN operations in the fault diagnosis field will also be studied.

References

- [1] J. Levine, X-31's loss (2004 (accessed September 21, 2020)).
URL http://www.nasa.gov/centers/dryden/news/X-Press/stories/2004/013004/new_x31.html
- [2] F. Bureau d'Enquetes et d'Analyses pour la securite de l'aviation civile, Paris, Report 3: on the accident on 1 june 2009 to the airbus a330-203 registered f-gzcp operated by air france flight af 447 rio de janeiro-paris (2011 (accessed September 21, 2020)).
URL <https://www.bea.aero/docspa/2009/f-cp090601e3.en/pdf/f-cp090601e3.en.pdf>
- [3] FAA, FAA Updates on Boeing 737 MAX (2020 (accessed 7 October, 2020)).
URL <https://www.faa.gov/news/updates/?newsId=93206>
- [4] P. Goupil, J. Boada-Bauxell, A. Marcos, E. Cortet, M. Kerr, H. Costa, Airbus efforts towards advanced real-time fault diagnosis and fault tolerant control, IFAC Proceedings Volumes 47 (3) (2014) 3471-3476.
- [5] E. Dubrova, Fault-tolerant design, Springer, 2013.
- [6] P. Goupil, Airbus state of the art and practices on FDI and FTC in flight control system, Control Engineering Practice 19 (6) (2011) 524-539.
- [7] E. Y. E. Y. Chow, A. Willsky, Analytical redundancy and the design of robust failure detection systems, IEEE Transactions on automatic control 29 (7) (1984) 603-614.
- [8] J. Marzat, H. Piet-Lahanier, F. Damongeot, E. Walter, Model-based fault diagnosis for aerospace systems: a survey, Proceedings of the Institution of Mechanical Engineers, Part G: Journal of Aerospace Engineering 226 (10) (2012) 1329-1360.
- [9] S. Hussain, M. Mokhtar, J. M. Howe, Sensor failure detection, identification, and accommodation using fully connected cascade neural network, IEEE Transactions on Industrial Electronics 62 (3) (2014) 1683-1692.

- [10] S. Hussain, M. Mokhtar, J. M. Howe, Aircraft sensor estimation for fault tolerant flight control system using fully connected cascade neural network, in: The 2013 International Joint Conference on Neural Networks (IJCNN), IEEE, 2013, pp. 1–8.
- [11] M. L. Fravolini, G. Del Core, U. Papa, P. Valigi, M. R. Napolitano, Data-driven schemes for robust fault detection of air data system sensors, IEEE Transactions on Control Systems Technology 27 (1) (2017) 234–248.
- [12] M. L. Fravolini, M. Rhudy, S. Gururajan, S. Cascianelli, M. Napolitano, Experimental evaluation of two pitot free analytical redundancy techniques for the estimation of the airspeed of an UAV, SAE International Journal of Aerospace 7 (2014-01-2163) (2014) 109–116.
- [13] S. Gururajan, M. L. Fravolini, H. Chao, M. Rhudy, M. R. Napolitano, Performance evaluation of neural network based approaches for airspeed sensor failure accommodation on a small UAV, in: 21st Mediterranean Conference on Control and Automation, IEEE, 2013, pp. 603–608.
- [14] R. Meyes, M. Lu, C. W. de Puiseau, T. Meisen, Ablation studies in artificial neural networks, arXiv preprint arXiv:1901.08644 (2019).
- [15] B. Zhou, A. Khosla, A. Lapedriza, A. Oliva, A. Torralba, Learning deep features for discriminative localization, in: Proceedings of the IEEE conference on computer vision and pattern recognition, 2016, pp. 2921–2929.
- [16] L. Van Eykeren, Q. Chu, Sensor fault detection and isolation for aircraft control systems by kinematic relations, Control Engineering Practice 31 (2014) 200–210.
- [17] M. Ariola, M. Mattei, I. Notaro, F. Corrado, A. Sollazzo, An SFDI observer-based scheme for a general aviation aircraft, International Journal of Applied Mathematics and Computer Science 25 (1) (2015) 149–158.

- [18] Q. He, W. Zhang, P. Lu, J. Liu, Performance comparison of representative model-based fault reconstruction algorithms for aircraft sensor fault detection and diagnosis, *Aerospace Science and Technology* 98 (2020) 105649.
- [19] P. Lu, L. Van Eykeren, E.-J. Van Kampen, Q. P. Chu, B. Yu, Adaptive hybrid unscented Kalman filter for aircraft sensor fault detection, isolation and reconstruction, in: *AIAA Guidance, Navigation, and Control Conference*, 2014, p. 1145.
- [20] P. Lu, L. Van Eykeren, E. Van Kampen, C. De Visser, Q. Chu, Adaptive three-step Kalman filter for air data sensor fault detection and diagnosis, *Journal of Guidance, Control, and Dynamics* 39 (3) (2016) 590–604.
- [21] P. Lu, L. Van Eykeren, E.-J. Van Kampen, Q. P. Chu, Air data sensor fault detection and diagnosis with application to real flight data, in: *AIAA Guidance, Navigation, and Control Conference*, 2015, p. 1311.
- [22] D. Berdjag, J. Cieslak, A. Zolghadri, Fault detection and isolation of aircraft air data/inertial system, *Progress in Flight Dynamics, Guidance, Navigation, Control, Fault Detection, and Avionics* 6 (2013) 317–332.
- [23] K. Rudin, G. J. Ducard, R. Y. Siegwart, A sensor fault detection for aircraft using a single Kalman filter and hidden Markov models, in: *2014 IEEE Conference on Control Applications (CCA)*, IEEE, 2014, pp. 991–996.
- [24] P. Freeman, P. Seiler, G. J. Balas, Air data system fault modeling and detection, *Control Engineering Practice* 21 (10) (2013) 1290–1301.
- [25] M. Mattei, G. Paviglianiti, Managing sensor hardware redundancy on a small commercial aircraft with H_∞ FDI observers, *IFAC Proceedings Volumes* 38 (1) (2005) 347–352.
- [26] F. Amato, C. Cosentino, M. Mattei, G. Paviglianiti, A direct/functional redundancy scheme for fault detection and isolation on an aircraft, *Aerospace Science and Technology* 10 (4) (2006) 338–345.

- [27] Y. Xue, Z. Zhen, L. Yang, L. Wen, Adaptive fault-tolerant control for carrier-based uav with actuator failures, *Aerospace Science and Technology* 107 (2020) 106227.
- [28] Y. Wan, T. Keviczky, Real-time fault-tolerant moving horizon air data estimation for the reconfigure benchmark, *IEEE Transactions on Control Systems Technology* 27 (3) (2018) 997–1011.
- [29] Y. Wan, T. Keviczky, M. Verhaegen, Robust air data sensor fault diagnosis with enhanced fault sensitivity using moving horizon estimation, in: 2016 American Control Conference (ACC), IEEE, 2016, pp. 5969–5975.
- [30] Y. Wan, T. Keviczky, Implementation of real-time moving horizon estimation for robust air data sensor fault diagnosis in the reconfigure benchmark, *IFAC-PapersOnLine* 49 (17) (2016) 64–69.
- [31] P. Castaldi, N. Mimmo, S. Simani, Avionic air data sensors fault detection and isolation by means of singular perturbation and geometric approach, *Sensors* 17 (10) (2017) 2202.
- [32] P. Castaldi, W. Geri, M. Bonfe, S. Simani, M. Benini, Design of residual generators and adaptive filters for the FDI of aircraft model sensors, *Control Engineering Practice* 18 (5) (2010) 449–459.
- [33] X. Zhu, J. Chen, Z. H. Zhu, Adaptive learning observer for spacecraft attitude control with actuator fault, *Aerospace Science and Technology* (2020) 106389.
- [34] P. Rosa, C. Silvestre, Fault detection and isolation of LPV systems using set-valued observers: An application to a fixed-wing aircraft, *Control Engineering Practice* 21 (3) (2013) 242–252.
- [35] L. Garbarino, G. Zazzaro, N. Genito, G. Fasano, D. Accardo, Neural network based architecture for fault detection and isolation in air data systems, in: 2013 IEEE/AIAA 32nd Digital Avionics Systems Conference (DASC), IEEE, 2013, pp. 2D4–1.

- [36] S. Gururajan, M. L. Fravolini, H. Chao, M. Rhudy, M. R. Napolitano, Performance evaluation of neural network based approaches for airspeed sensor failure accommodation on a small UAV, in: 21st Mediterranean Conference on Control and Automation, IEEE, 2013, pp. 603–608.
- [37] A. Abbaspour, P. Aboutalebi, K. K. Yen, A. Sargolzaei, Neural adaptive observer-based sensor and actuator fault detection in nonlinear systems: Application in UAV, *ISA Transactions* 67 (2017) 317–329.
- [38] M. L. Fravolini, M. R. Napolitano, G. Del Core, U. Papa, Experimental interval models for the robust fault detection of aircraft air data sensors, *Control Engineering Practice* 78 (2018) 196–212.
- [39] Y. Dong, J. Tao, Y. Zhang, W. Lin, J. Ai, Deep learning in aircraft design, dynamics, and control: Review and prospects, *IEEE Transactions on Aerospace and Electronic Systems* (2021).
- [40] H. A. Talebi, K. Khorasani, S. Tafazoli, A recurrent neural-network-based sensor and actuator fault detection and isolation for nonlinear systems with application to the satellite’s attitude control subsystem, *IEEE Transactions on Neural Networks* 20 (1) (2008) 45–60.
- [41] M. Chen, P. Shi, C.-C. Lim, Adaptive neural fault-tolerant control of a 3-DOF model helicopter system, *IEEE Transactions on Systems, Man, and Cybernetics: Systems* 46 (2) (2015) 260–270.
- [42] E. Sobhani-Tehrani, H. A. Talebi, K. Khorasani, Hybrid fault diagnosis of nonlinear systems using neural parameter estimators, *Neural Networks* 50 (2014) 12–32.
- [43] Y. Dong, An application of deep neural networks to the in-flight parameter identification for detection and characterization of aircraft icing, *Aerospace Science and Technology* 77 (2018) 34–49.

- [44] Y. Dong, Implementing deep learning for comprehensive aircraft icing and actuator/sensor fault detection/identification, *Engineering Applications of Artificial Intelligence* 83 (2019) 28–44.
- [45] B. Eroglu, M. C. Sahin, N. K. Ure, Autolanding control system design with deep learning based fault estimation, *Aerospace Science and Technology* 102 (2020) 105855.
- [46] Y. Lin, J.-w. Zhang, H. Liu, Deep learning based short-term air traffic flow prediction considering temporal–spatial correlation, *Aerospace Science and Technology* 93 (2019) 105113.
- [47] Microsoft, NNI, <https://github.com/microsoft/nni>.
- [48] J. Bergstra, R. Bardenet, Y. Bengio, B. Kégl, Algorithms for hyperparameter optimization, *Advances in neural information processing systems* 24 (2011).
- [49] R. R. Selvaraju, M. Cogswell, A. Das, R. Vedantam, D. Parikh, D. Batra, Grad-CAM: Visual explanations from deep networks via gradient-based localization, in: *Proceedings of the IEEE international conference on computer vision*, 2017, pp. 618–626.
- [50] A. Chattopadhyay, A. Sarkar, P. Howlader, V. N. Balasubramanian, Grad-CAM++: Generalized gradient-based visual explanations for deep convolutional networks, in: *2018 IEEE winter conference on applications of computer vision (WACV)*, IEEE, 2018, pp. 839–847.
- [51] D. Omeiza, S. Speakman, C. Cintas, K. Weldermariam, Smooth Grad-CAM++: An enhanced inference level visualization technique for deep convolutional neural network models, *arXiv preprint arXiv:1908.01224* (2019).
- [52] H. Wang, Z. Wang, M. Du, F. Yang, Z. Zhang, S. Ding, P. Mardziel, X. Hu, Score-CAM: score-weighted visual explanations for convolutional neural networks, in: *Proceedings of the IEEE/CVF conference on computer vision and pattern recognition workshops*, 2020, pp. 24–25.

- [53] H. Wang, R. Naidu, J. Michael, S. S. Kundu, SS-CAM: smoothed score-CAM for sharper visual feature localization, arXiv preprint arXiv:2006.14255 (2020).
- [54] H. G. Ramaswamy, et al., Ablation-CAM: Visual explanations for deep convolutional network via gradient-free localization, in: Proceedings of the IEEE/CVF Winter Conference on Applications of Computer Vision, 2020, pp. 983–991.
- [55] Y. LeCun, J. S. Denker, S. A. Solla, Optimal brain damage, in: Advances in neural information processing systems, 1990, pp. 598–605.
- [56] S. Han, H. Mao, W. J. Dally, Deep compression: Compressing deep neural networks with pruning, trained quantization and huffman coding, arXiv preprint arXiv:1510.00149 (2015).
- [57] W. Wen, C. Wu, Y. Wang, Y. Chen, H. Li, Learning structured sparsity in deep neural networks, Advances in neural information processing systems 29 (2016) 2074–2082.
- [58] Y. Guo, A. Yao, Y. Chen, Dynamic network surgery for efficient dnns, arXiv preprint arXiv:1608.04493 (2016).
- [59] G. Hinton, O. Vinyals, J. Dean, Distilling the knowledge in a neural network, arXiv preprint arXiv:1503.02531 (2015).
- [60] J. Gou, B. Yu, S. J. Maybank, D. Tao, Knowledge distillation: A survey, International Journal of Computer Vision 129 (6) (2021) 1789–1819.
- [61] R. Bardenet, B. Kégl, Surrogating the surrogate: accelerating gaussian-process-based global optimization with a mixture cross-entropy algorithm, in: 27th International Conference on Machine Learning (ICML 2010), Omnipress, 2010, pp. 55–62.
- [62] D. C. Montgomery, Design and analysis of experiments, John wiley & sons, 2017.

- [63] J. Bergstra, Y. Bengio, Random search for hyper-parameter optimization., *Journal of machine learning research* 13 (2) (2012).
- [64] S. Falkner, A. Klein, F. Hutter, BOHB: Robust and efficient hyperparameter optimization at scale, in: *International Conference on Machine Learning*, PMLR, 2018, pp. 1437–1446.
- [65] K. Deb, A. Anand, D. Joshi, A computationally efficient evolutionary algorithm for real-parameter optimization, *Evolutionary computation* 10 (4) (2002) 371–395.
- [66] F. Hutter, H. H. Hoos, K. Leyton-Brown, Sequential model-based optimization for general algorithm configuration, in: *International conference on learning and intelligent optimization*, Springer, 2011, pp. 507–523.
- [67] Y. Dong, Y. Zhang, J. Ai, Full-altitude attitude angles envelope and model predictive control-based attitude angles protection for civil aircraft, *Aerospace Science and Technology* 55 (2016) 292–306.
- [68] L. Höhndorf, J. Siegel, J. Sembiring, P. Koppitz, F. Holzapfel, Reconstruction of aircraft states during landing based on quick access recorder data, *Journal of Guidance, Control, and Dynamics* 40 (9) (2017) 2393–2398.
- [69] R. C. Nelson, et al., *Flight stability and automatic control*, Vol. 2, WCB/McGraw Hill New York, 1998.
- [70] V. Klein, T. R. Ratvasky, B. R. Cobleigh, Aerodynamic parameters of High-Angle-of attack Research Vehicle (HARV) estimated from flight data, Tech. rep. (1990).
- [71] Department of Defense, *Flying Qualities of Piloted Aircraft* (1997 (accessed October 20, 2020)).
URL https://cafe.foundation/v2/pdf_tech/Flying.Qualities/PAV.FlyQual.Mil1797A.pdf

- [72] Y. Zhang, H. Zhao, J. Ma, Y. Zhao, Y. Dong, J. Ai, A deep neural network-based fault detection scheme for aircraft imu sensors, *International Journal of Aerospace Engineering* 2021 (2021).
- [73] I. Goodfellow, A. Courville, and Y. Bengio, *Deep learning*, Vol. 1, MIT press Cambridge, 2016.
- [74] Y. Dong, Deep learning-based opponent aircraft attitude detection in autonomous air combat, *Journal of Aerospace Information Systems* 16 (4) (2019) 162–167.
- [75] K. Simonyan, A. Zisserman, Very deep convolutional networks for large-scale image recognition, *arXiv preprint arXiv:1409.1556* (2014).
- [76] K. He, X. Zhang, S. Ren, J. Sun, Deep residual learning for image recognition, in: *Proceedings of the IEEE conference on computer vision and pattern recognition*, 2016, pp. 770–778.
- [77] C. Shorten, T. M. Khoshgoftaar, A survey on image data augmentation for deep learning, *Journal of Big Data* 6 (1) (2019) 1–48.
- [78] P. Molchanov, S. Tyree, T. Karras, T. Aila, J. Kautz, Pruning convolutional neural networks for resource efficient inference, *arXiv preprint arXiv:1611.06440* (2016).
- [79] NVIDIA, Jetson Nano, <https://www.nvidia.com/en-us/autonomous-machines/embedded-systems/jetson-nano/>.
- [80] D. R. Jones, A taxonomy of global optimization methods based on response surfaces, *Journal of global optimization* 21 (4) (2001) 345–383.
- [81] J. S. Bergstra, R. Bardenet, Y. Bengio, B. Kégl, Algorithms for hyperparameter optimization, in: *Advances in neural information processing systems*, 2011, pp. 2546–2554.